Supporting Information

Peptide Nucleic Acid-Clicked Ti₃C₂Tₓ MXene for Ultrasensitive Enzyme-free Electrochemical Detection of microRNA Biomarkers

Muhsin Ali[1], Sharat Chandra Barman[1], Erol Hasan[1], Mohamed Nejib Hedhili[2], Husam N. Alshareef[1], and Dana Alsulaiman[1, *]

[1] Material Science and Engineering, Physical Science and Engineering Division, King Abdullah University of Science & Technology (KAUST), Thuwal, 23955-6900, Saudi Arabia

[2] Imaging and Characterization Core Lab, King Abdullah University of Science and Technology, Thuwal, 23955-6900, Saudi Arabia

[*] Corresponding author; email: dana.alsulaiman@kaust.edu.sa

Contents

Experimental section

Materials: All miRNA oligonucleotides were purchased from Integrated DNA Technologies (IDT). Other chemical reagents including (3-azidopropyl) triethoxysilane (Gelest, 98%), $[Ru(NH_3)_6]Cl_3$, phosphate buffered saline, alumina powder (1, 0.3, and 0.05 μm), potassium chloride (KCl, 99.0%), and TE buffer were purchased from Sigma Aldrich. Ethanol and buffer salts were of analytical grade. Millipore-purified deionized (DI) water was used throughout the experiments. Fmoc-Rink amide MBHA resin, ethyl 2-cyano-2-(hydroxyimino)acetate (Oxyma), and Fmoc-Arg-(Pbf)-OH were obtained from Gyros Protein Technologies. Fmoc/Bhoc-protected PNA monomers were obtained from PolyOrg, Inc. DBCO-C6-NHS ester was obtained from BroadPharm. Acetonitrile (ACN; Optima™ LC/MS and HPLC grades), formic acid (LC/MS grade), and *N*,*N*-dimethylformamide (DMF, ACS reagent) were obtained from Thermo Fisher Scientific. *N*,*N'*-Diisopropylcarbodiimide (DIC), piperidine solution (20% in DMF), and triisopropylsilane (TIPS, 99%) were obtained from Sigma-Aldrich. Diethyl ether (HPLC grade) and trifluoroacetic acid (TFA, GPR grade) were obtained from VWR Chemicals. Dichloromethane (DCM, HPLC grade) was obtained from Honeywell Research Chemicals. DBCO-functionalized PNA probes were synthesized in our lab following solid-phase peptide synthesis protocols using Fmoc chemistry as described below. Serum from human male AB plasma was purchased commercially from Sigma-Aldrich (H4522-100mL). The protocol detailing serum usage was approved by the KAUST Institutional Bioethics and Biosafety Committee under protocol 22IBEC028.

Synthesis, Purification, and Validation of the DBCO–PNA Probes: The PNA sequences were synthesized at a 0.02-mmol scale on Rink-amide MBHA resin (0.358 mmol/g) using a PurePep™Chorus automated peptide synthesizer. Their chemical structures are shown in Figure S7(A, and B). The synthesis was conducted using a standard Fmoc solid-phase synthesis protocol including systematically repeated steps of coupling and deprotection interspaced with washings (3 × 2 mL DMF). The coupling was conducted in two cycles of heating at 85°C for 5 min four equivalents of Fmoc-amino acid and DIC/Oxyma as coupling reagents in DMF (4 mL). Deprotection was performed in two cycles of heating at 65°C with 20% piperidine in DMF (3 mL) for 40 s.The N-terminus capping of PNA with DBCO-C6-NHS ester was conducted on resin in a syringe using a polypropylene frit (20 μm). After swelling for 30 min in DMF (3 mL) followed by solvent draining, the resin was mixed with a preprepared solution of PBA-NHS ester (4 eq.) and *N*-methylmorpholine (8 eq.) in DMF (3 mL) and allowed to react under gentle shaking overnight at RT. The reaction was stopped by draining the reaction mixture, and the resin was washed with DMF (3 × 5 mL) and DCM (5 × 5 mL) and vacuum dried.

PNA was cleaved from the resin using a cleavage cocktail of TFA/TIPS/water (95:2.5:2.5% v/v/v) at RT for 2.5 h. The resin was removed by filtration, and the filtrate was precipitated in ice-cold diethyl ether. The precipitate was isolated by centrifugation (4000 rpm, 10 min, 4°C), dissolved in ACN/water (70:30 v/v%), and then freeze-dried. The crude PNA product was purified by semipreparative reversed-phase HPLC on a Shimadzu LC-20 HPLC system equipped with a C18 column (5 μm, 30 mm × 250 mm) using 0.1% formic

acid in water (A) and 0.1% formic acid in ACN (B) as the eluents. Semipreparative runs were performed by applying a linear gradient (at 35 mL/min) of 10% to 80% B over 30 min. Fractions collected during the HPLC purification were analyzed by reversed-phase liquid chromatographic–electrospray ionization mass spectrometry (LC-ESI-MS) on a LC-IDX Tribrid Orbitrap mass spectrometer equipped with a C18 column (3.5 μm, 30 mm × 250 mm) eluting with 0–100% B gradient over 20 min at 0.5 mL/min. The fractions containing exclusively the desired product (i.e., above 90%) were pooled and freeze-dried. The PNA identity and purity were confirmed by comparing the observed and calculated m/z (ESI$^+$) values for the two PNA probes as follows:

7-mer of DBCO-PNA: 1310.08 ([2618.7 + 2H]$^{2+}$ = 1,310.35), 873.71 ([2618.7 + 3H]$^{3+}$ = 873.9), 655.44 ([2618.7 + 4H]$^{4+}$= 655.68), 524.63 ([2618.7 + 5H]$^{5+}$= 524.74)

17-mer of DBCO-PNA: 1,306.29 ([5222.2 + 4H]$^{4+}$ = 1,306.55), 1045.24 ([5222.2 + 5H]$^{5+}$= 1,045.44), 871.20 ([5222.2 + 6H]$^{6+}$= 871.36), 746.88 (5222.2 + 7H]$^{7+}$= 747.02).

Oligonucleotide Sequences

Oligonucleotides	*Sequence 5' to 3' or C-terminal to N-terminal*
7-mer PNA	CATTTCT-Arg-Arg-DBCO
17-mer PNA	TGTGACAGACCATTTCT-Arg-Arg-DBCO
hsa-miR-141	5' UAACACUGUCUGGUAAAGAUGG 3'
miR-141-1SNP	5' UAACAAUGUCUGGUAAAGAUGG 3'
miR-141-2SNPs	5' UAACAAUGUCUGGUAUAGAUGG 3'
miR-141-3SNPs	5' UAAGACUGUCUGCUAAAGUUGG 3'
Cel-miR-39	5' UCACCGGGUGUAAAUCAGCUUG 3'

Synthesis of Bare MXene (Ti$_3$C$_2$T$_x$): MXene nanosheets were prepared following our published protocols.[36] Briefly, 3:3:3 mL of HCl, HF (47–51%), and cold DI water were mixed and stirred for 5 min at 200 rpm. MAX powder (1 g) purchased commercially was gradually added to the etchant solution while stirring using a Teflon magnetic bar. Cold DI water (3 mL) was added to the suspension, which was then etched for ~17 h in an oil bath at 40 °C at 500 rpm, followed by several cycles of centrifugation with DI water at 2600 rpm for 5 min until a pH of 5–6 was obtained. Next, a LiCl (1 g/35 mL DI) solution was added to the precipitant and magnetically stirred for 30 min. The precipitant was washed with DI water multiple times until the solution reached a pH of 5–6. Finally, the solution was centrifuged several times at 500 rpm for 10 min and the supernatant was collected as ultrathin Ti$_3$C$_2$-MXene nanosheets.

Azido–MXene Preparation: The as-synthesized ultrathin Ti_3C_2 MXene nanosheets were treated with AzPTES to introduce azide functional groups via a silanization reaction, as shown in Figure S2. Herein, 16 mg of Ti_3C_2 nanosheets were prepared in 8mL of ethanol, into which the silane coupling agent (160 µL) was added dropwise with magnetic stirring at 500 rpm at RT for 48 h. The AzPTES silane linker reacts with the hydroxyl terminations of $Ti_3C_2T_x$. Next, the suspension was washed three times with ethanol and water (1:1) by centrifugation at 3500 rpm to remove the unreacted silane coupling agents from the AzPTES–$Ti_3C_2T_x$ nanosheets. The final suspension of AzPTES–modified $Ti_3C_2T_x$ (Azido-MXene) nanosheets was subsequently dried in a vacuum oven at 50°C for 12 h. The obtained product, Azido-MXene, was kept in a desiccator at RT until further use. Before proceeding with the click reaction, the Azido–MXene was suspended in 1 mL of ethanol and sonicated to obtain a homogeneous solution.

Copper-free click Reaction between Azido–MXene and DBCO–PNA: click chemistry was used as a high-yield bio-orthogonal strategy to functionalize the PNA probe onto the MXene nanosheets. To achieve a 2:1 molar excess of DBCO to azide functionality, 5 mg of azido–MXene was reacted with 19 mg of DBCO-functionalized PNA in DI water under stirring for 12 h at RT. The product was washed three times with DI to remove any unbound PNA molecules, and the final product (PNA–MXene nanosheet) was stored at RT/4°C until further use.

Preparation of MXene–PNA-coated GCE (WE): A GCE was used as the working electrode in a three-electrode electrochemical setup to study the electrochemical performance and properties of azido–MXene . For miRNA sensing, the GCE was polished with commercial alumina slurry of 0.3 and 0.05 µm, in turn, and then sonicated with a 1:1 mixture of acetone and DI water, followed by rinsing with DI water and drying under nitrogen flow. Next, 4 µl of the MXene–PNA nanosheet was drop-casted on the 2-mm GCE. The electrode was left to dry at RT in a laminar flow cabinet, and the MXene–PNA showed high binding affinity to and stability on the electrode surface. The MXene–PNA-coated GCE bioelectrode was then used as the working electrode in further electrochemical studies. The working electrode modifications are shown in Scheme 1.

Data Analysis: Statistical analysis and data plotting were conducted using OriginPro software.

Table S1. Electrochemical nucleic acid biosensors for detection of cancer-related biomarkers
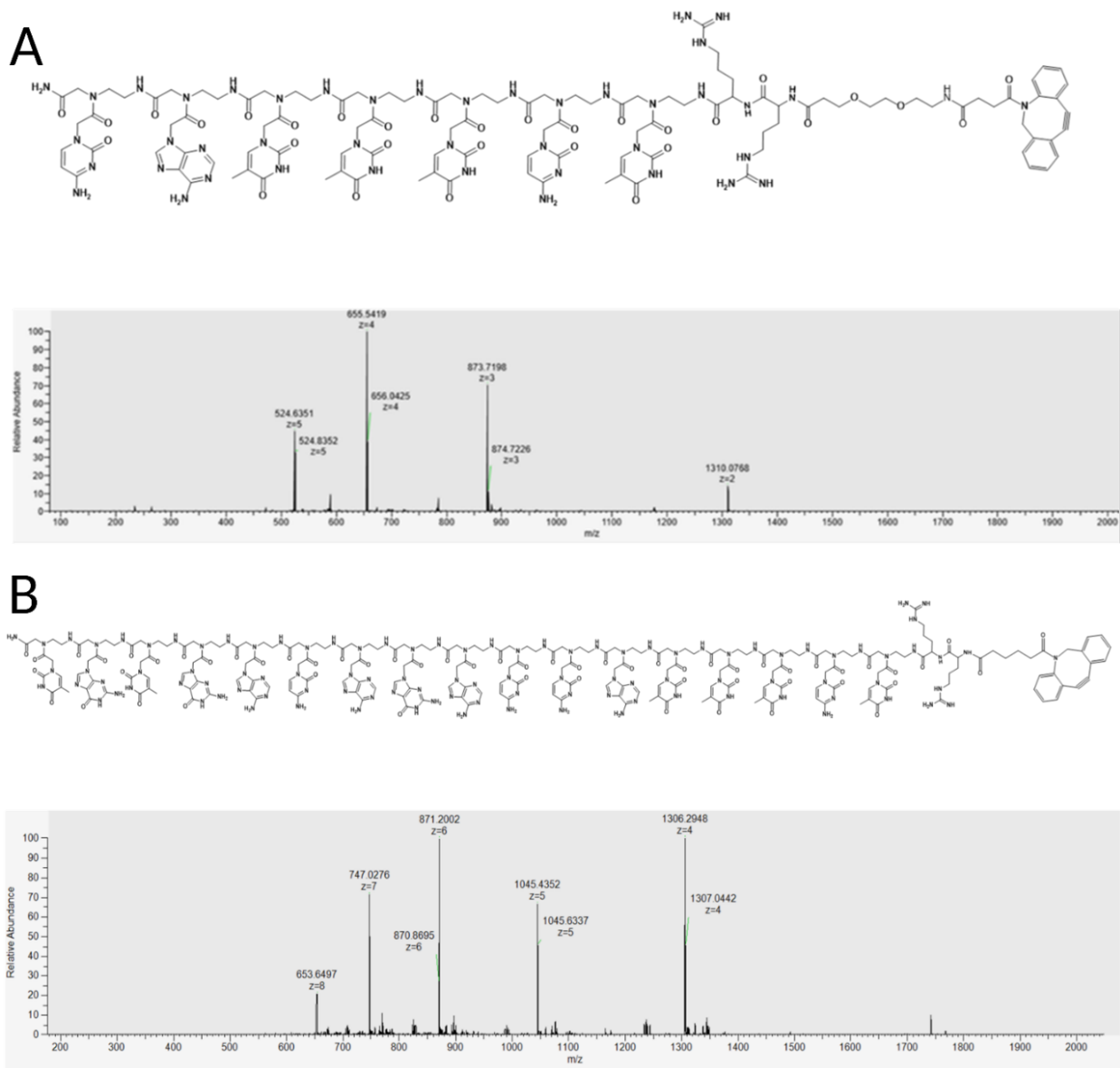
Materials	Bioreceptor Probe	Amplification Strategy	LOD	Dynamic range	Reference
Reduced graphene oxide/gold (rGO/Au) composite	ssDNA	None	1.73 pM	10 µM–10 pM	[1]
Popcorn-like gold nanofilms	ssDNA	None	2.2 fM	0.5 fM – 0.5 pM	[2]
Nanozymes	ssDNA	HRP*	43 aM	100 aM –100 pM	[3]
2D MnO$_2$ Nanoflakes as Nanozymes	ssDNA	Oxidase-like Nanozyme (MnO$_2$)	0.25 nM	0.4–140 nM	[4]
AuNPs*	Hairpin DNA	CHA*	0.34 fM	100 fM – 1 nM	[5]
conductive molecules (polyaniline)	TDN*	HRP*	0.29 fM	1 fM to 1 nM	[6]
Au deposited GCE	Hairpin DNA	RCA* + DNAzyme	36 aM	100 aM to 10 nM	[7]
P$_L$-Cys/MoS$_2$	ssDNA	None	78 fM	100 fM – 1 nM	[8]
Fe$_3$O$_4$ MNPs*-IL-rGO-AuNPs	ssDNA	DSN-assisted target recycling and magnetic separation enrichment	2.1 fM	5 fM-50 nM	[9]
polydopamine nanoparticles (MPDA)	ssDNA	SDR*	362 fM	1 pM – 1nM	[10]
MXene-PNA nanoconstruct	**PNA**	**None**	**40 aM**	**100 aM – 1 nM**	**This work**

Acronyms: HRP = Horseradish Peroxidase enzyme; CHA: Catalytic Hairpin Assembly; RCA= Rolling Circle Amplification; TDN = tetrahedral DNA Nanoconstruct; AuNPs= Gold nanoparticles; MNPs = Magnetic Nanoparticles; SDR= Strand Displacement Reaction

The above table highlights the recent advances in electrochemical biosensors for the detection of miRNA. As seen, to achieve attomolar sensitivity (i.e., sub-100 aM limits of detection), existing approaches in the literature **require the use of amplification or enzymes**. The reported strategies that do not require enzymes for amplification typically rely on 0D nanomaterials and nanomaterial composites, **but these fail to achieve sufficient sensitivity**. Furthermore, most approaches rely upon the use of natural oligonucleotide probes (**mainly ssDNA) as bioreceptor**s which are often only physically immobilized on the nanomaterial surfaces and offer **poor robustness and susceptibility to degradation** by enzymes and extreme physicochemical conditions.

In contrast, this work achieves attomolar sensitivity without the use of enzymes, amplification strategies, or composites with other nanomaterials. The excellent sensitivity of this work can be attributed to a synergistic interplay of intrinsic and engineered elements, including: (i) the inherent high conductivity and electron transport properties of MXene nanosheets, (ii) their distinctive nanoporous morphology facilitating bioreceptor loading and efficient electron transfer, and (iii) the formation of a stable and direct covalent bond through the click-based functionalization between the bioreceptor and the MXene surface. The specificity and robustness of our biosensor arises from the use of synthetic PNA probes as opposed to their natural counterparts which are prone to degradation.

S1. Chemical structure and Mass Spectra of the 7-mer and 17-mer PNA probes (DBCO-PNA)

A

B

Figure S1. A. Chemical structure and ESI-MS spectrum in positive mode of the **7-mer** PNA which is N-end modified with DBCO. B. Chemical structure and ESI-MS spectrum in positive mode of the **17-mer** PNA which is N-end modified with DBCO.

S2. Schematic illustration of the functionalization strategy of bare MXene to produce PNA-MXene
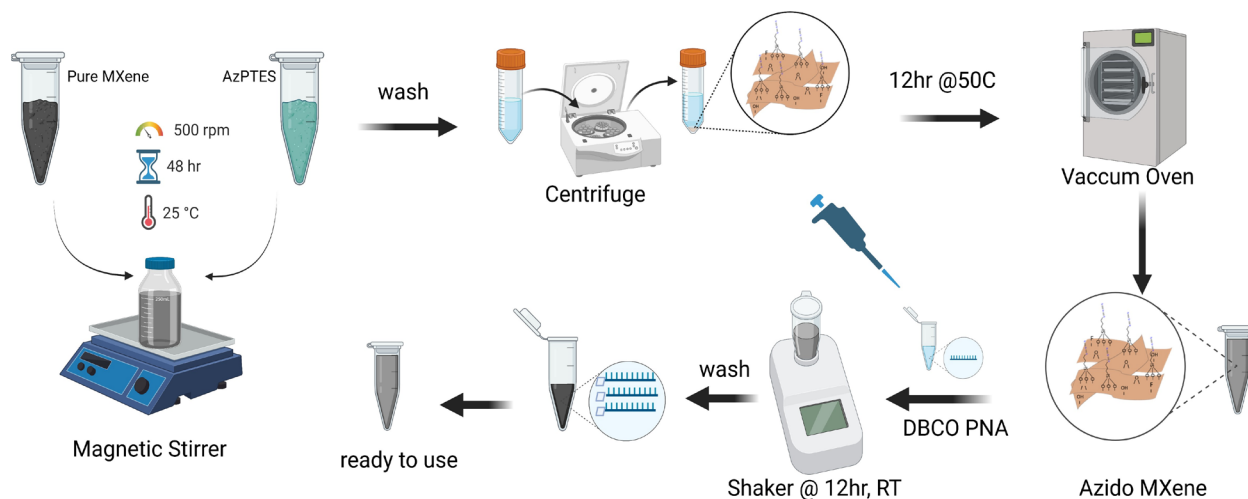
Figure S2. Schematic illustration of the functionalization strategy of bare or pure MXene to produce PNA-MXene. Notably, the strategy involves two major steps: azido functionalization of MXene using AzPTES in ethanol followed by conjugation with DBCO–PNA using bio-orthogonal copper-free click chemistry in distilled water.
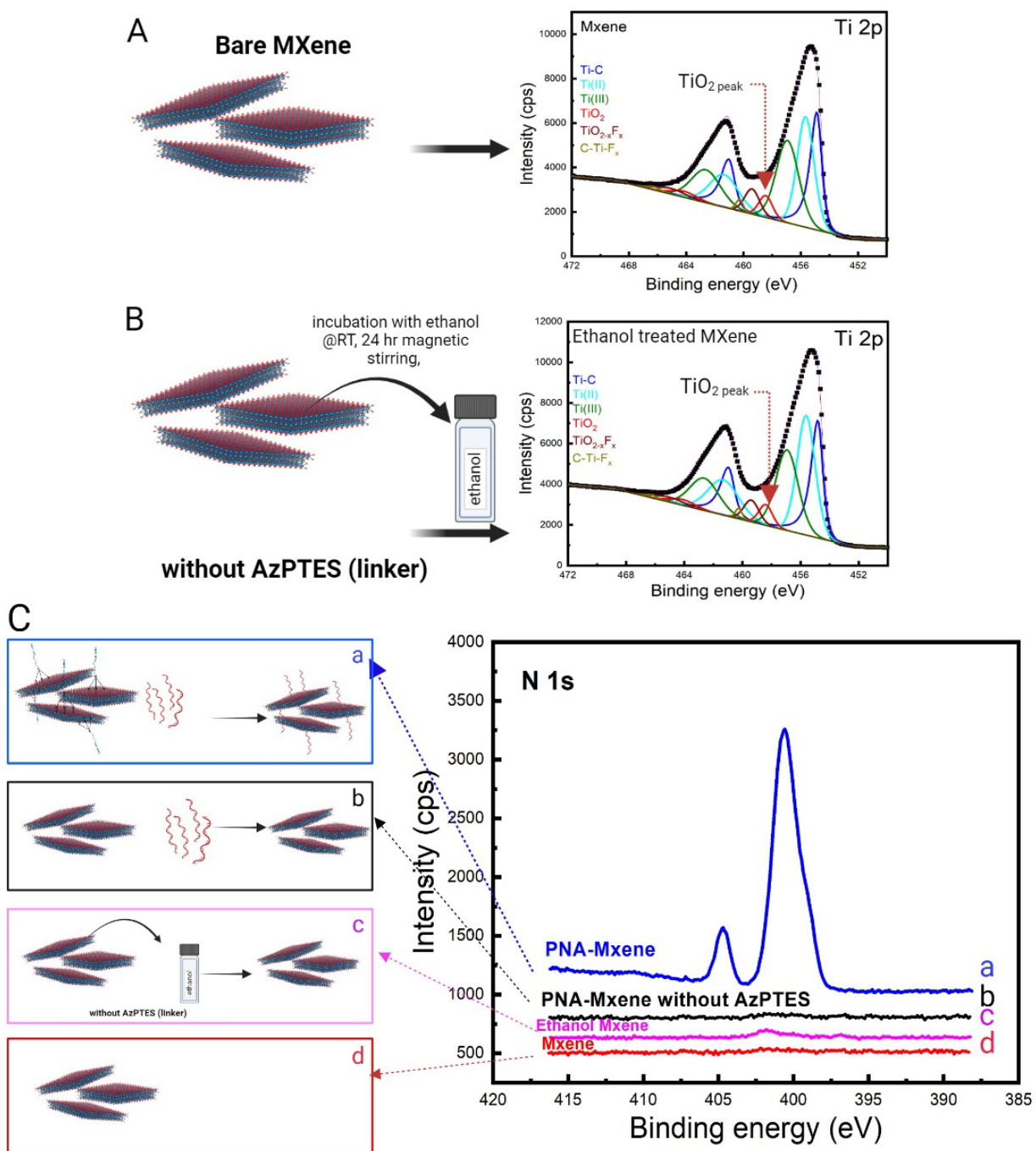
S3. XPS Spectra of the Bare MXene, AzPTES, Azido-MXene and DBCO-PNA

The Ti 2p core-level spectrum of the bare MXene sample was fitted with six doublets (Ti 2p $2p_{3/2}$–Ti $2p_{1/2}$) with a fixed area ratio of 2:1 and a doublet separation of 5.7 eV (except for Ti–C, for which the doublet separation was 6.2 eV). The Ti $2p_{3/2}$ components were located at 454.9, 455.7, 456.9, 458.4, 459.3, and 460.3 eV as shown in Figure (S3, B). The Ti $2p_{3/2}$ component centered at 454.8 eV corresponded to Ti bound to C[11,12]. The Ti $2p_{3/2}$ components centered at 455.7 and 457.0 eV can be attributed to Ti ions with valence states of 2^+ and 3^+, respectively[13]. The Ti $2p_{3/2}$ component centered at 458.5 eV corresponded to TiO$_2$.[13] The Ti $2p_{3/2}$ components centered at 459.3 and 460.3 eV corresponded to Ti from TiO$_{2-x}$F$_x$ species and C–Ti–F$_x$ bond, respectively. The C 1s core-level spectrum of the bare MXene sample was fitted with seven components located at 281.8, 282.6, 284.3, 284.8, 286.4, 288.1, and 290.0 eV corresponding to C–Ti, C–Ti–O, C=C (sp^2), C–C/C–H (sp^3), C–O, C=O, and O–C=O and C–F bonds, respectively as shown in Figure S3, A.[14] The wide spectrum of the AzPTES is shown in Figure 1S, C. The Si 2p spectra for the AzPTES and Azido–MXene is shown in Figure S3 (D, E). Wide spectrum of PNA probe, along with C1s core-level XPS spectrum of PNA, and O 1s core-level XPS spectrum with fittings of PNA is shown in Figure S3 (F, G, H).
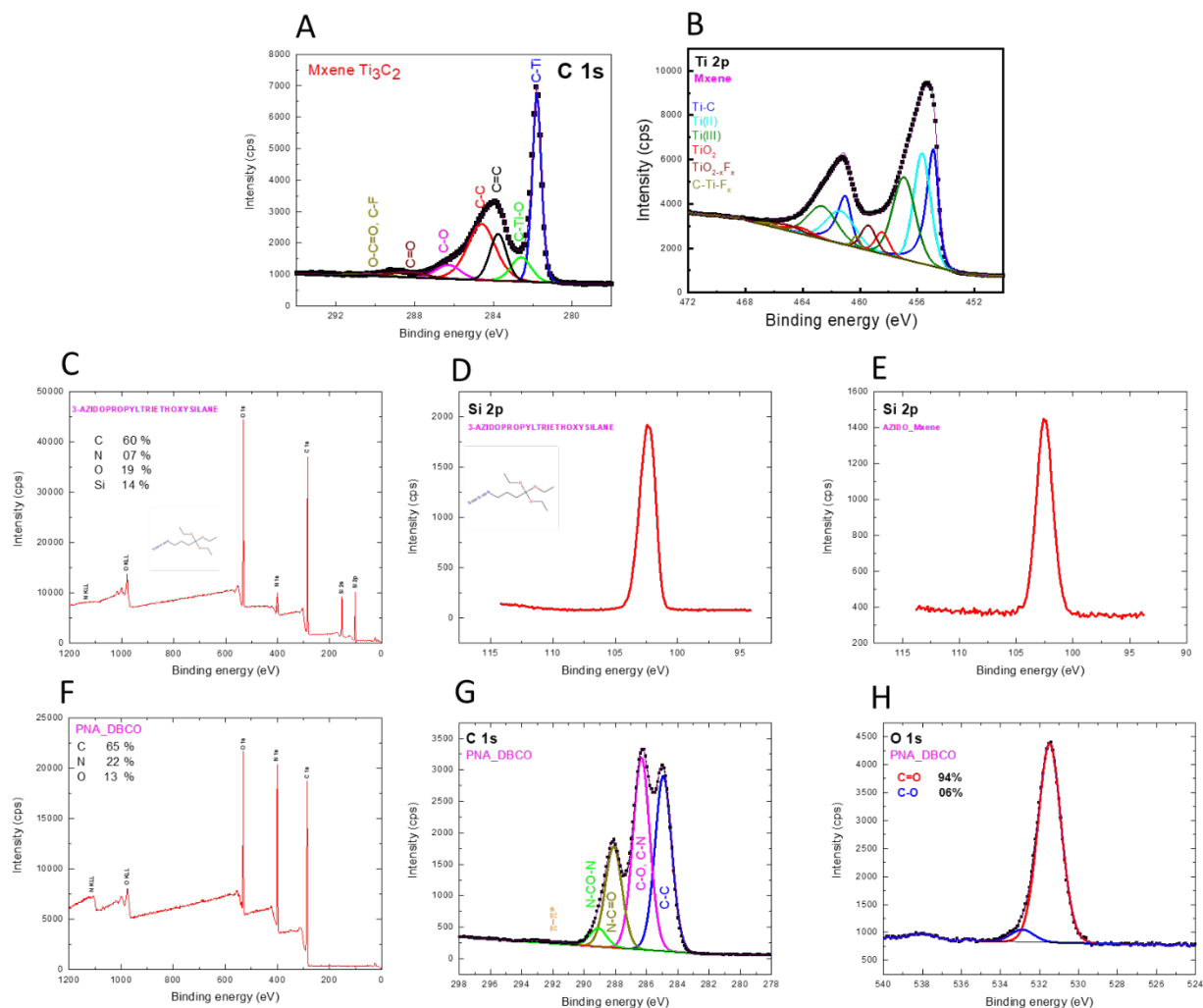
Figure S3. A. C 1s and B. Ti 2p core-level spectra of the bare MXene sample **C.** XPS survey spectrum of 3-azidepropyltriethoxysilane (AzPTES), D. Si 2p core-level XPS spectrum of 3-azidepropyltriethoxysilane (AzPTES), E. Si 2p core-level XPS spectrum of azido-MXene, F. XPS wide spectrum of the 17-mer PNA probe (DBCO-PNA), G. C 1s core-level XPS spectrum of the PNA, and H. O 1s core-level XPS spectrum with fittings of PNA.

S4. Control Experiments to Confirm Ti–O–Si Bond and Covalent Bonding of PNA on MXene Surface

Figure S4. Control Experiments to Confirm Ti–O–Si Bond and Covalent Bonding of PNA on MXene Surface. (A) XPS spectra of the bare MXene. (B) XPS spectra of the bare MXene undergone identical conditions without the AzPTES with the peaks for Ti highlighted in red. (C) N 1s core-level spectra of the bare Mxene (red), Mxene without AzPTES (pink), PNA-MXene without the AzPTES (black) and PNA-Mxene (blue) respectively, along with the schematic representation.

Table S2. Atomic Percentage of the various elements obtained from XPS analysis of Bare MXene, Azido-MXene and PNA-MXene

Table S1. Atomic Percentage of various elements obtained from XPS analysis

	Bare MXene			Azido_MXene			PNA_Mxene		
	At%	FWHM	Area	At%	FWHM	Area	At%	FWHM	Area
Ti	26	2.88	82339	8	5.67	17687	4	3.14	8149
C	44	4.81	19599	42	2.84	12194	56	3.68	18228
O	15	3.29	19136	25	3.58	20180	17	2.74	15340
F	13	2.16	20619	3	2.27	3422	1	2.19	1233
Cl	1	2.78	2271	1	2.65	350	1	3.44	256
N	1	2.48	613	13	3.25	6292	19	2.70	10788
Si				9	2.36	2972	3	2.39	1104

Table S3. XPS Analysis Surface Composition Table showing atomic percentage of the Ti species in the four samples: bare MXene, MXene treated with ethanol, Azido-MXene and PNA-MXene

Composition	Species	binding energies	bare MXene	bare MXene treated with ethanol	Azido-MXene	PNA-Mxene
			%	%	%	%
Ti 2p	Ti-C	454.9	27	28	18	23
	Ti(II)	455.7	31	31	25	28
	Ti(III)	456.9	30	30	24	26
	TiO_2 / Ti-O-Si	458.4	5	5	28	15
	$TiO_{2-x}F_x$	459.4	6	5	3	5
	C-Ti-F_x	460.3	1	1	2	3
	total Ti%		100	100	100	100

S5. Zeta potential of bare MXene and azido-MXene along with the DLS of bare MXene nanosheets
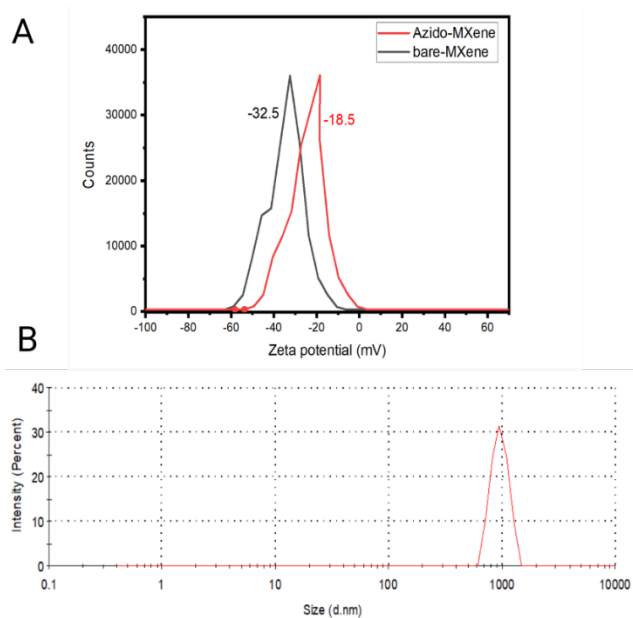
Figure S5. (A) Zeta potential of bare MXene (black) and Azido-MXene (red) along. B. DLS of bare MXene nanosheets showing an average size of 1.4± 0.08µm

S6. EDX mapping of bare MXene, Azido-MXene, and PNA–MXene


Bare MXene   **Azido-MXene**   **PNA-MXene**
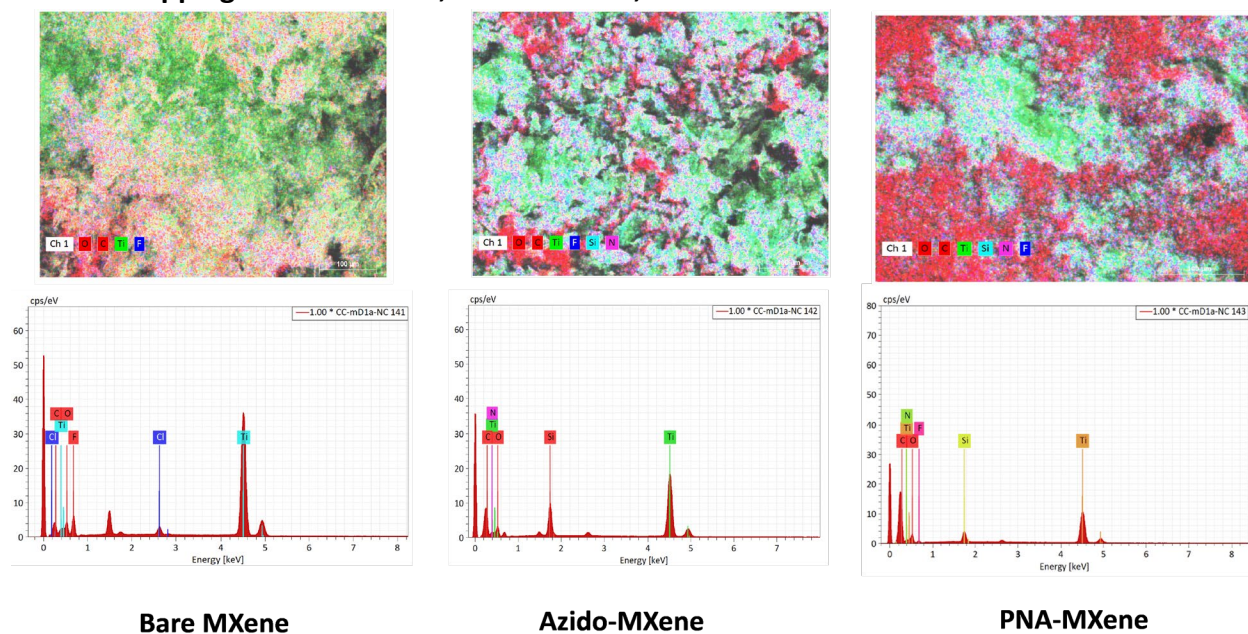
Figure S6. EDX mapping of bare MXene, azido-MXene, and PNA–MXene. The presence of additional elements (Si and N) after each step confirms the successful modification and immobilization of PNA via Cu-free click reaction.

S7. AFM Analysis of MXene and PNA-MXene

Atomic force microscopy (AFM, Bruker, Dimension Icon SPM) was used to characterize the surface topography and quantify the thickness of individual MXene nanosheets (Figure S7, A) and PNA-MXene nanosheets (Figure S7, B). For the PNA-MXene sample, the AFM scan reveals a two-step profile: a first step of ~10 nm, representing the combined thickness of PNA and MXene (MXene t + PNA t) from the bottom surface (step height 1), and a second step of ~7 nm, roughly corresponding to the thickness of the PNA layer (PNA t) on the top surface of the MXene sheet (step height 2).
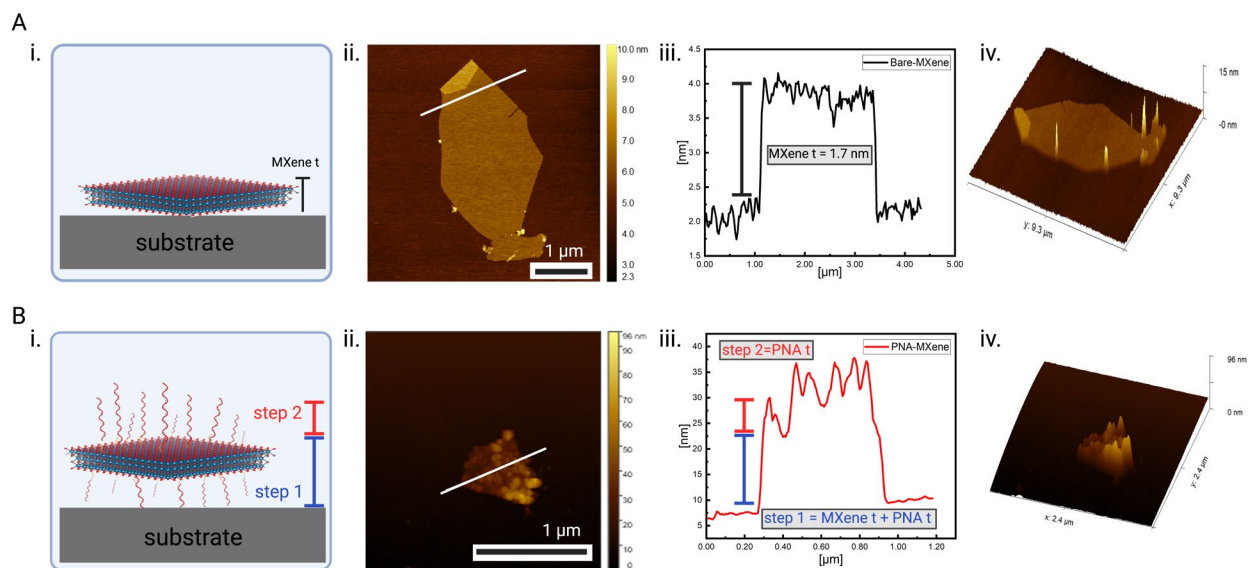
Figure S7. AFM surface analysis of A. Bare MXene and B. PNA-MXene nanoconstruct (details), showing: i. schematic illustrations of the materials on a substrate with labels defining MXene thickness 'MXene t', 'step 1' and 'step 2' heights. ii. AFM scans, iii. line profile of the nanosheet, iv. 3D topographical images constructed from (ii). *Step 1 (measured ~10 nm) shown in blue was associated with the combined thickness of a single MXene sheet and the bottom layer of PNA. Step 2 (measured ~ 7nm) was associated with the thickness of a single PNA layer including silane linker, estimated to be ~7nm.*

S8. Electrochemical characterization of the MXene-coated GCE
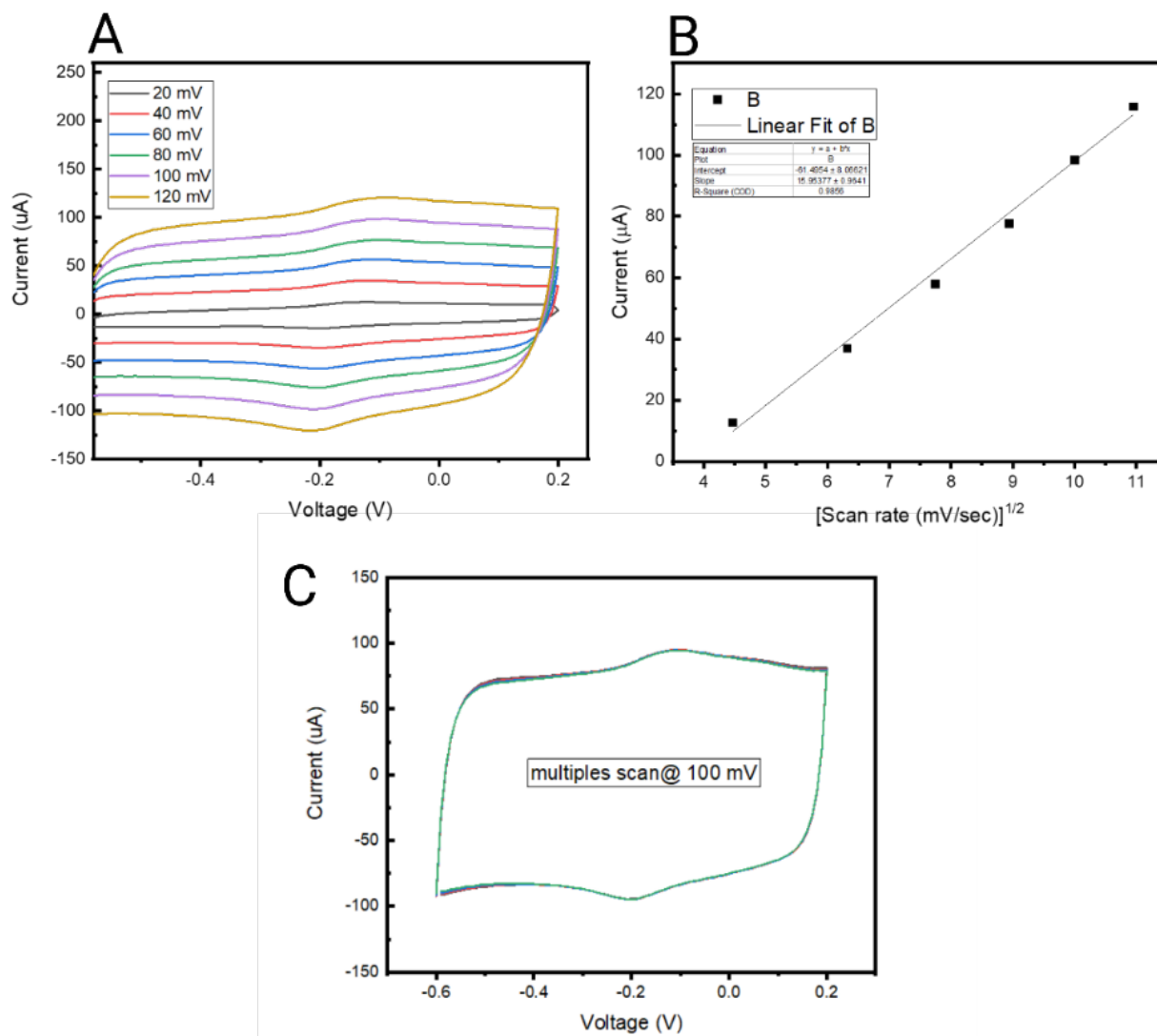
Figure S8. A. Cyclic voltammogram scans of the MXene-coated GCE at scan rates ranging from 20 to 120 mV s^{-1} B. The cathodic and anodic currents increased linearly with the square root of the scan rate, indicating a reversible and diffusion-controlled redox reaction. C. Five repeated scans of the MXene-coated GCE with a standard deviation of 0.026 of the anodic peak current, demonstrating overlap of the CVs and hence the electrochemical stability of the MXene on GCE.

S9. Proposed mechanism behind the sensor's superior analytical performance

The superior analytical performance of our biosensor achieving attomolar sensitivity in the absence of enzymes, amplification mechanisms, or additional 0D nanomaterials, can be attributed to the interplay between two synergistic effects, afforded by our novel PNA-MXene transducing material (Figure S9A) when compared to a standard planar electrode (Figure S9B). The combination of these two effects increases the probability of hybridization events and the efficiency of electron transfer between the redox probe-intercalated duplex and the electrode surface. Both aforementioned synergistic effects are discussed in detail below:

1. Increased probe grafting density due to biofunctionalization efficiency:

    The high efficiency and bio-orthogonality of our click chemistry-based functionalization approach ensures that PNA probes are densely and uniformly immobilized on the 3D porous MXene surface (as validated by XPS and EDX surface analysis) (Figure S9, i). This higher grafting density increases the probability of hybridization events (PNA:miRNA duplex formation) (Figure S9, ii), leading to increased MB intercalation, and thus increased efficiency of redox reactions. The importance of probe grafting density has been highlighted by previous work which states that once inside the porous structure, the probability of hybridization events increases significantly with increased probe grafting density (Daggumati, Matharu, and Seker 2015).

1. Unique geometric effects limiting Debye volume and enhancing the efficiency of electron transfer:

    Previous studies have demonstrated that nanoporous electrode structures can significantly enhance sensor sensitivity due to increased specific surface area. For example, a comparison between planar and porous gold electrodes showed an enhancement factor of 9.26 in electroactive surface area, ultimately increasing the current in nanoporous gold films by 10 times compared to planar gold. This agrees with the findings of other studies where nanostructured electrodes enhanced the sensitivity of aptamer-based electrochemical sensors (Li et al. 2020; Downs et al. 2021), In our system, we observed an increase in faradic current (~15.5 µA compared to 2.24 µA) between the bare GCE and MXene-coated GCE electrodes. This increase corresponded to a 7-fold enhancement in the electrochemically active surface which was attributed to two main properties of the MXene nanosheets: the unique 3D porous morphology of our nanocomposite material on the GCE surface (increasing specific surface area) and its intrinsic electronic conductivity.

    In concert with these geometric effects, the superior sensitivity of our platform may also arise from altered charge screening effects within the porous architecture of our PNA-MXene transducing material, which can be explained by the concept of "Debye volume" first introduced by Shoorideh et al in 2014.[15] It has been shown that limiting Debye volume at an electrode surface can extend the electric double layer (EDL) into solution, reducing charge screening effects at that interface.[16,17] This effect has also been shown to reduce the LOD of sensors with nanostructured electrodes by 4-fold relative to planar electrodes with the same footprint. [18] In our system, decreasing Debye volume within the porous structure leads to more efficient electron transfer (by weakening charge screening) and an increase in the probability of faradaic electron transfer events for a given probe conformation, resulting in enhanced sensitivity (Figure S9, iii). This effect is supported by our experimental findings whereby increasing bioreceptor probe

length above the theoretical Debye length of ~1.4 nm enhances sensitivity, which would not be the case for planar electrodes. This also indicates that our EDL extends beyond the estimated Debye length, and limiting Debye volume within the confines of the porous transducing material enables more efficient electron transfer from duplex-intercalated MB.
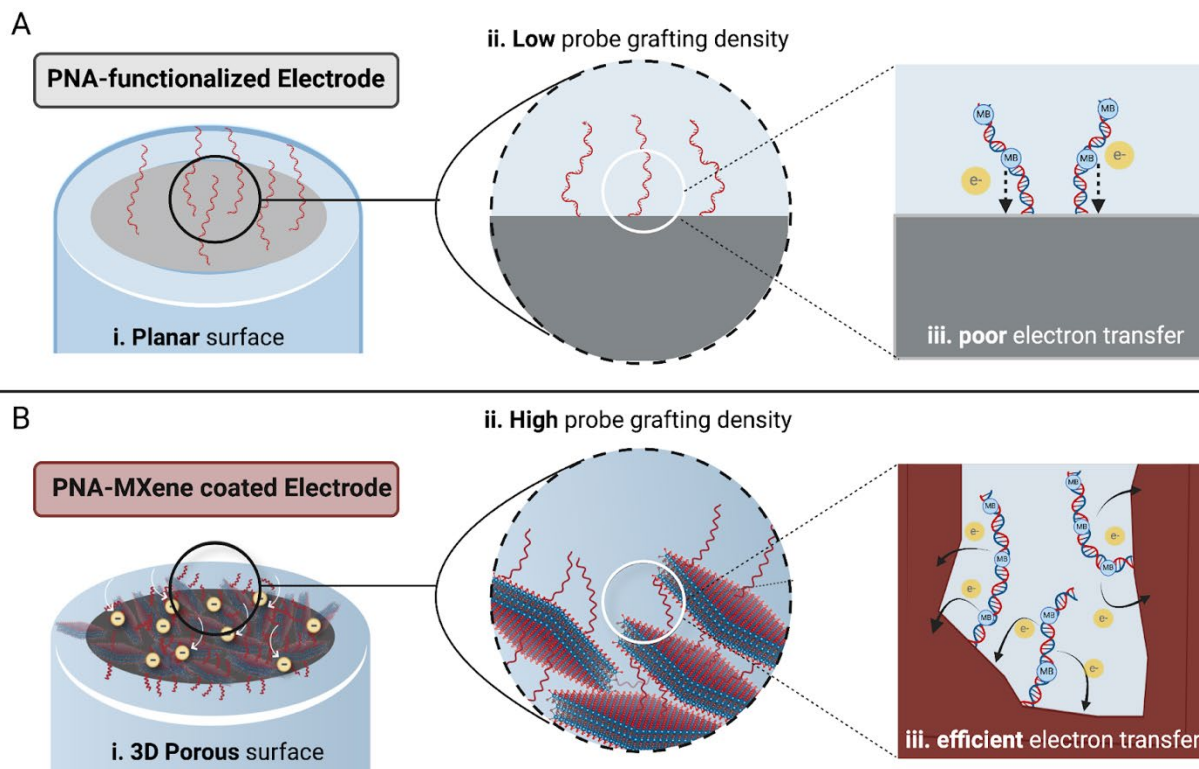
Figure S9. Schematic illustrations depicting the proposed mechanism behind the superior analytical performance of our biosensor based on a PNA-MXene transducing material. Comparison between a standard planar electrode functionalized with PNA (A) versus an electrode coated with our new PNA-MXene transducing material (B) in terms of i. surface morphology, ii. probe grafting density, and iii. efficiency of electron transfer.

Overall, enhanced probe grafting density in concert with the intrinsic electrical conductivity and unique morphology of our PNA-MXene transducing material altogether contribute to elucidating the mechanism behind our platform's superior analytical performance.

References

[1]   S. Kasturi, Y. Eom, S. R. Torati, C. Kim, *Journal of Industrial and Engineering Chemistry* **2021**, *93*, 186.

[2]   H. Zhou, J. Zhang, B. Li, J. Liu, J.-J. Xu, H.-Y. Chen, *Anal Chem* **2021**, *93*, 6120.

[3]   H. Zhang, M. Fan, J. Jiang, Q. Shen, C. Cai, J. Shen, *Anal Chim Acta* **2019**, *1064*, 33.

[4]   J. Wu, W. Lv, Q. Yang, H. Li, F. Li, *Biosens Bioelectron* **2021**, *171*, 112707.

[5]   T. Lee, M. Mohammadniaei, H. Zhang, J. Yoon, H. K. Choi, S. Guo, P. Guo, J. Choi, *Advanced Science* **2020**, *7*, DOI 10.1002/advs.201902477.

[6]   T. Guo, Y. Xiang, H. Lu, M. Huang, F. Liu, M. Fang, J. Liu, Y. Tang, X. Li, F. Yang, *ACS Appl Mater Interfaces* **2022**, *14*, 18209.

[7]   T.-L. Hou, L. Zhu, X.-L. Zhang, Y.-Q. Chai, R. Yuan, *Anal Chem* **2022**, *94*, 10524.

[8]   Y. Yao, H. Pan, Y. Luo, D. Zhu, J. Chao, S. Su, L. Wang, *Analyst* **2021**, *146*, 1663.

[9]   M. Yin, J. Jiao, L. Lu, B. Hu, L. Xue, F. Dai, X. Wang, Z. Wang, T. Wang, Q. Chen, *Biosens Bioelectron* **2024**, *249*, 116009.

[10]   X. Xie, Z. Wang, M. Zhou, Y. Xing, Y. Chen, J. Huang, K. Cai, J. Zhang, *Small Methods* **2021**, *5*, DOI 10.1002/smtd.202101072.

[11]   Y. Dall'Agnese, M. R. Lukatskaya, K. M. Cook, P.-L. Taberna, Y. Gogotsi, P. Simon, *Electrochem commun* **2014**, *48*, 118.

[12]   J. Zhu, Y. Tang, C. Yang, F. Wang, M. Cao, *J Electrochem Soc* **2016**, *163*, A785.

[13]   J. Halim, K. M. Cook, M. Naguib, P. Eklund, Y. Gogotsi, J. Rosen, M. W. Barsoum, *Appl Surf Sci* **2016**, *362*, 406.

[14]   J. Halim, M. R. Lukatskaya, K. M. Cook, J. Lu, C. R. Smith, L.-Å. Näslund, S. J. May, L. Hultman, Y. Gogotsi, P. Eklund, M. W. Barsoum, *Chemistry of Materials* **2014**, *26*, 2374.

[15]   P. Daggumati, Z. Matharu and E. Seker, *Anal. Chem.*, 2015, **87**, 8149–8156.

[16]   K. Shoorideh and C. O. Chui, *Proc. Natl. Acad. Sci. U. S. A.*, 2014, **111**, 5111–5116.

[17]   V. Kesler, B. Murmann and H. T. Soh, *ACS Nano*, 2020, **14**, 16194–16201.

[18]   K. Fu, J.-W. Seo, V. Kesler, N. Maganzini, B. D. Wilson, M. Eisenstein, B. Murmann and H. T. Soh, *Adv. Sci.*, 2021, **8**, e2102495.